



<b>Publication Year</b>	2017
<b>Acceptance in OA</b>	2020-08-04T09:51:02Z
<b>Title</b>	Dark matter distribution in X-ray luminous galaxy clusters with Emergent Gravity
<b>Authors</b>	ETTORI, STEFANO, Ghirardini, V., Eckert, D., Dubath, F., Pointecouteau, E.
<b>Publisher's version (DOI)</b>	10.1093/mnrasl/slx074
<b>Handle</b>	<a href="http://hdl.handle.net/20.500.12386/26682">http://hdl.handle.net/20.500.12386/26682</a>
<b>Journal</b>	MONTHLY NOTICES OF THE ROYAL ASTRONOMICAL SOCIETY
<b>Volume</b>	470

# Dark matter distribution in X-ray luminous galaxy clusters with Emergent Gravity

S. Ettori,<sup>1,2★</sup> V. Ghirardini,<sup>1,3</sup> D. Eckert,<sup>4</sup> F. Dubath<sup>4</sup> and E. Pointecouteau<sup>5,6</sup>

<sup>1</sup>INAF, Osservatorio Astronomico di Bologna, via Pietro Gobetti 93/3, I-40129 Bologna, Italy

<sup>2</sup>INFN, Sezione di Bologna, viale Berti Pichat 6/2, I-40127 Bologna, Italy

<sup>3</sup>Dipartimento di Fisica e Astronomia, Università di Bologna, via Pietro Gobetti 93/2, I-40129 Bologna, Italy

<sup>4</sup>Department of Astronomy, University of Geneva, ch. d'Ecogia 16, CH-1290 Versoix, Switzerland

<sup>5</sup>CNRS, IRAP, 9 Av. colonel Roche, BP 44346, F-31028 Toulouse cedex 4, France

<sup>6</sup>UPS-OMP, IRAP, Université de Toulouse, F-31028 Toulouse, France

Accepted 2017 May 9. Received 2017 May 8; in original form 2016 December 22

## ABSTRACT

We present the radial distribution of the dark matter in two massive, X-ray luminous galaxy clusters, Abell 2142 and Abell 2319, and compare it with the quantity predicted as apparent manifestation of the baryonic mass in the context of the ‘Emergent Gravity’ scenario, recently suggested from Verlinde. Thanks to the observational strategy of the *XMM–Newton* Cluster Outskirt Programme (X-COP), using the X-ray emission mapped with *XMM–Newton* and the Sunyaev–Zel’dovich signal in the *Planck* survey, we recover the gas density, temperature and thermal pressure profiles up to  $\sim R_{200}$ , allowing us to constrain at an unprecedented level the total mass through the hydrostatic equilibrium equation. We show that, also including systematic uncertainties related to the X-ray-based mass modelling, the apparent ‘dark’ matter shows a radial profile that has a shape different from the traditional dark matter distribution, with larger discrepancies (by a factor of 2–3) in the inner ( $r < 200$  kpc) cluster’s regions and a remarkable agreement only across  $R_{500}$ .

**Key words:** galaxies: clusters: individual: Abell 2142 – galaxies: clusters: individual: Abell 2319 – galaxies: clusters: intracluster medium – dark matter – X-rays: galaxies: clusters.

## 1 INTRODUCTION

The distribution of the gravitating mass in galaxy clusters is one of the key ingredients to use them as astrophysical laboratories and cosmological probes (see e.g. Allen, Evrard & Mantz 2011; Kravtsov & Borgani 2012). In the present favourite  $\Lambda$  cold dark matter ( $\Lambda$ CDM) scenario, galaxy clusters are dominated by dark matter (80 per cent of the total mass), with a contribution in the form of hot plasma emitting in X-ray and detectable through the Sunyaev–Zel’dovich (SZ; Sunyaev & Zel’dovich 1972) effect (about 15 per cent of the total mass, i.e.  $M_{\text{DM}}/M_{\text{gas}} \sim 4\text{--}7$ ) and the rest in stars (few per cent; see e.g. Gonzalez et al. 2013). Although an intriguing and plausible explanation to the observed gravitational effects induced from galaxy clusters, the still unknown nature of the dark matter invites to consider alternative scenarios.

In this Letter, we present and discuss the application of one such alternative model, the ‘Emergent Gravity’ theory proposed recently in Verlinde (2016), to the mass distribution in X-ray luminous galaxy clusters. The ‘Emergent Gravity’ theory is a theoretical framework in which space–time and gravity emerge together from

the entanglement structure of an underlying microscopic theory. Although a description of the cosmology is not yet available for this theory, where, in the approximation used by Verlinde, the dark energy dominates our universe and ordinary matter leads only to small perturbations, the use of an effective  $\Lambda$ CDM background cosmology to convert angular into physical scales is still a reasonable approximation at the low-redshift regime where we operate. For the  $\Lambda$ CDM model, we adopt the cosmological parameters  $H_0 = 70 \text{ km s}^{-1} \text{ Mpc}^{-1}$  and  $\Omega_m = 1 - \Omega_\Lambda = 0.3$ . In a similar context, the ‘Emergent Gravity’ theory has already shown a good capability to reproduce the observed signal of the galaxy–galaxy lensing profiles (Brouwer et al. 2016) and the velocity dispersion profiles of eight dwarf spheroidal satellites of the Milky Way (Diez-Tejedor et al. 2016).

In this study, we refer often to radii,  $R_\Delta$ , and masses,  $M_\Delta$ , that are the corresponding values estimated at the given overdensity  $\Delta$  as  $M_\Delta = 4/3 \pi \Delta \rho_{c,z} R_\Delta^3$ , where  $\rho_{c,z} = 3H_z^2/(8\pi G)$  is the critical density of the universe at the observed redshift  $z$  of the cluster and  $H_z = H_0 [\Omega_\Lambda + \Omega_m(1+z)^3]^{0.5}$  is the value of the Hubble constant at the same redshift.

This Letter is organized as follows. In Section 2, we describe the ‘Emergent Gravity’ scenario and how an apparent dark matter distribution can be associated with the observed baryonic mass. In

\* E-mail: stefano.ettori@oabo.inaf.it

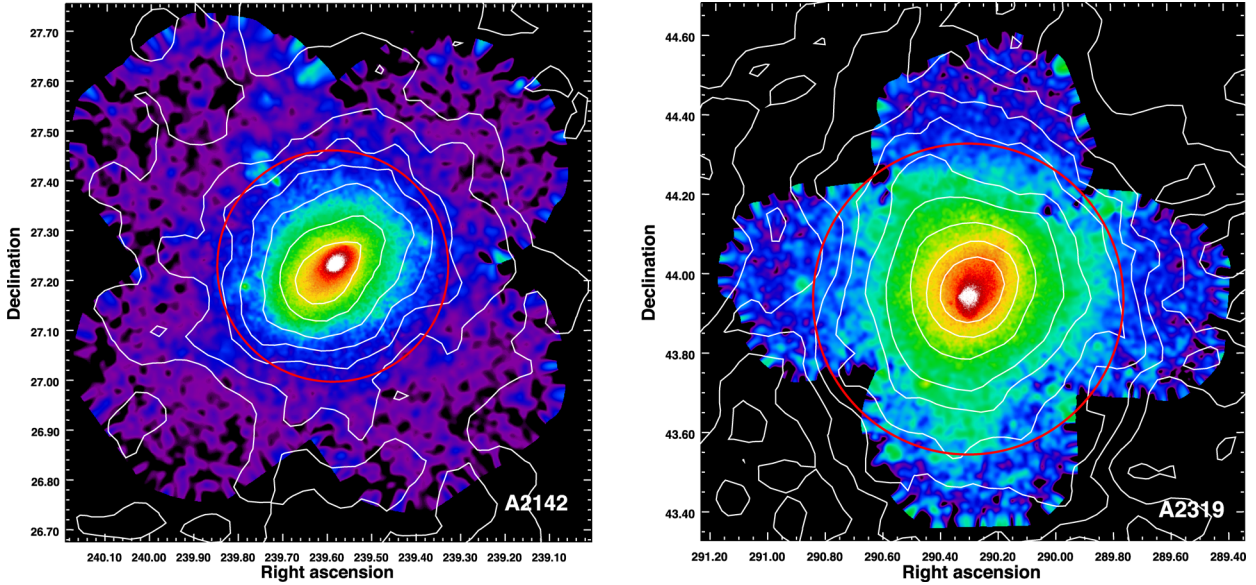


**Figure 1.** Particle-background-subtracted, adaptively smoothed and vignetting-corrected *XMM–Newton* mosaic images of X-COP clusters in the [0.7–1.2] keV band of Abell 2142 (left-hand panel) and Abell 2319 (right-hand panel). The corresponding Planck Compton-parameter contours are shown in white. The contour levels correspond to 1, 3, 5, 7, 10, 15, 20, 30, 40 and  $50\sigma$ . The red circles indicate the estimated value of  $R_{500}$ .

Section 3, we present the dark matter profiles reconstructed through techniques based on X-ray and SZ data only in two massive galaxy clusters that are part of the *XMM–Newton* Cluster Outskirt Programme (X-COP) sample, an *XMM–Newton* Large Programme that targets the outer regions of a sample of 13 massive clusters in the redshift range 0.04–0.1 at uniform depth. In Section 4, we compare these dark matter profiles with the ones recovered through ‘Emergent Gravity’, assessing the systematic uncertainties affecting the X-ray mass measurements, and summarize our main findings in Section 5. Unless mentioned otherwise, the quoted errors are statistical uncertainties at a  $1\sigma$  confidence level.

## 2 APPARENT DARK MATTER IN THE EMERGENT GRAVITY

In the ‘Emergent Gravity’, dark matter can appear as manifestation of an additional gravitational force describing the ‘elastic’ response due to the entropy displacement, and with a strength that can be described in terms of the Hubble constant and of the baryonic mass distribution for a spherically symmetric, static and isolated astronomical system as (equation 7.40 in Verlinde 2016)

$$\int_0^r \frac{G M_{\text{DM,EG}}^2(r')}{r'^2} dr' = \frac{M_{\text{B}}(r) c H_0 r}{6}. \quad (1)$$

By operating the derivatives with respect to the radius of the two terms, and rearranging the quantities to isolate the dark matter component  $M_{\text{DM}}$ , it is straightforward to show that the following relation holds:

$$\begin{aligned} M_{\text{DM,EG}}^2(r) &= \frac{cH_0}{6G} r^2 \frac{d(M_{\text{B}}(r)r)}{dr} \\ &= \frac{cH_0}{6G} r^2 \left( M_{\text{B}}(r) + r \frac{dM_{\text{B}}(r)}{dr} \right) \\ &= \frac{cH_0}{6G} r^2 (M_{\text{B}}(r) + 4\pi r^3 \rho_{\text{B}}(r)) \\ &= \frac{cH_0}{6G} r^2 M_{\text{B}}(r) (1 + 3\delta_{\text{B}}), \end{aligned} \quad (2)$$

where  $M_{\text{B}}(r) = \int_0^r 4\pi \rho_{\text{B}} r'^2 dr' = M_{\text{gas}}(r) + M_{\text{star}}(r)$  is the baryonic mass equal to the sum of the gas and stellar masses, and  $\delta_{\text{B}}$  is equal to  $\rho_{\text{B}}(r)/\bar{\rho}_{\text{B}}$ , with  $\bar{\rho}_{\text{B}} = M_{\text{B}}(r)/V(<r)$  representing the mean baryonic density within the spherical volume  $V(<r)$ . In our case, the gas mass has been obtained from the integral over the cluster’s volume of the gas density that is obtained from the geometrical deprojection of the observed surface brightness (Fig. 1), including a careful treatment of the background subtraction. This allows us to resolve the signal out to about  $R_{200}$ . The stellar mass has been estimated by using a Navarro–Frenk–White (NFW, Navarro, Frenk & White 1997) profile with a concentration of 2.9 (see e.g. Lin, Mohr & Stanford 2004) and by requiring  $M_{\text{star}}(<R_{500})/M_{\text{gas}}(<R_{500}) = 0.39 (M_{500}/10^{14} M_{\odot})^{-0.84}$  (Gonzalez et al. 2013).

It is worth noting that equation (2) can be expressed as an acceleration  $g_{\text{EG}}$  depending on the acceleration  $g_{\text{B}}$  induced from the baryonic mass:

$$\begin{aligned} g_{\text{EG}} &= G \frac{M_{\text{DM,EG}} + M_{\text{B}}}{r^2} \\ &= g_{\text{B}} (1 + y^{-1/2}), \end{aligned} \quad (3)$$

where  $y = 6/(cH_0) \times g_{\text{B}}/(1 + 3\delta_{\text{B}})$ . Equation (3) takes a form very similar to the one implemented in MOND (e.g. Milgrom & Sanders 2016) with a characteristic acceleration  $a_0 = cH_0(1 + 3\delta_{\text{B}})/6$ .

## 3 DARK MATTER WITH THE HYDROSTATIC EQUILIBRIUM EQUATION

We evaluate how the apparent dark matter profile described in equation (2) reproduces the mass distribution recovered by using the hydrostatic equilibrium equation applied to two massive, X-ray luminous galaxy clusters that are part of the X-COP sample. The X-COP (Eckert et al. 2017) has been built to target the outer regions of a sample of 13 massive clusters ( $M_{500} > 3 \times 10^{14} M_{\odot}$ ) in the redshift range 0.04–0.1 at uniform depth. The sample was selected based on the signal-to-noise ratio in the *Planck* SZ survey

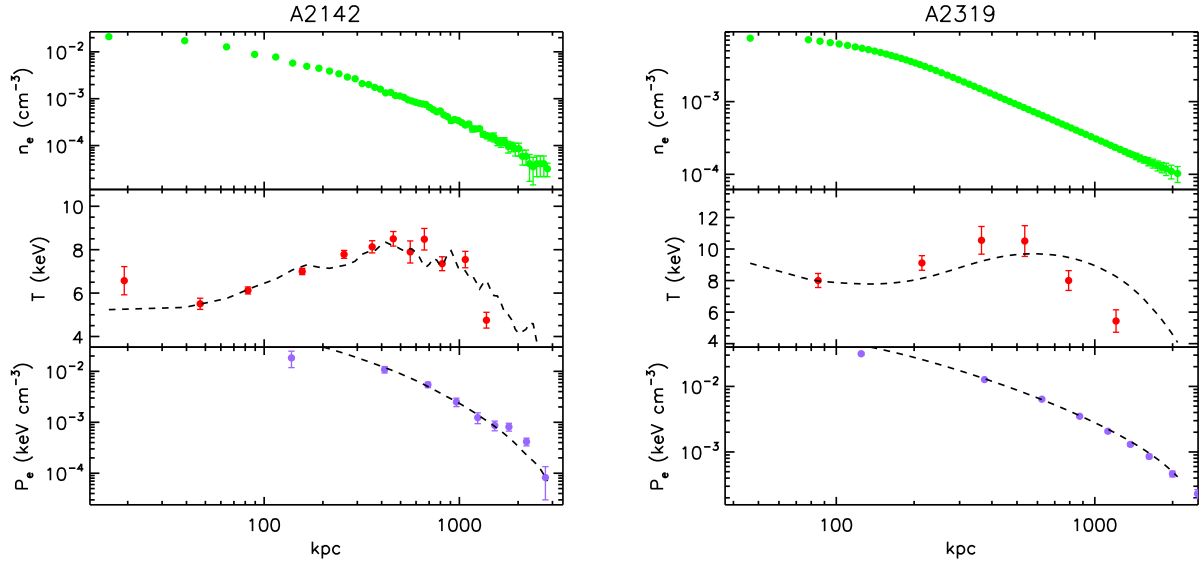


**Figure 2.** From the top to bottom: observed deprojected electron density, temperature and SZ pressure profiles, with the statistical error bars overplotted. The dashed lines indicate the temperature and pressure profiles required from the best-fitting NFW mass model for the given gas density profile (see Section 3).

(Planck Collaboration I 2011) with the aim of combining high-quality X-ray and SZ constraints throughout the entire cluster volume. Our observing strategy allows us to reach a sensitivity of  $3 \times 10^{-16}$  erg cm $^{-2}$  s $^{-1}$  arcmin $^{-2}$  in the [0.5–2.0] keV range, thanks to a good control of systematic uncertainties. The two objects in question, Abell 2142 and Abell 2319, are the first targets of the X-COP sample for which the complete *XMM-Newton* analysis of their gas properties out to  $R_{200}$  has been completed (see Fig. 1). Abell 2142 ( $z = 0.091$ ) shows a relatively relaxed morphology extended along the south-east/north-west (SE/NW) axis, and is undergoing some minor mergers in its outskirts (Owers, Nulsen & Couch 2011; Eckert et al. 2014). This cluster was mapped in the framework of X-COP pilot project (Tchernin et al. 2016). Abell 2319 ( $z = 0.056$ ; Struble & Rood 1999) is also a massive system in which the galaxy distribution indicates that it is a merger of two main components with a 3:1 mass ratio, the smaller system being located  $\sim 10$  arcmin north of the main structure (Oegerle, Hill & Fitchett 1995). The cluster exhibits a prominent cold front SE of the main core (Ghizzardi, Rossetti & Molendi 2010) and a giant radio halo (Farnsworth et al. 2013; Storm et al. 2015). This is one of the most significant SZ detections in the Planck catalogue (Planck Collaboration XXIX 2014), and its complete X-ray analysis, combined with the SZ pressure profile and resolved in eight azimuthal sectors, will be presented in a forthcoming paper (Ghirardini et al., in preparation). Considering the merging state of this galaxy cluster, we present here the analysis performed in the most relaxed sector, the one enclosed between position angles  $180^\circ$  and  $225^\circ$ . Under a reasonable approximation, these clusters are following Verlinde’s prescriptions for the validity of the Emergent Gravity modelling: They are reasonably spherical, quite isolated (being not embedded in the potential well of any neighbour objects and with no major mass accretion) and with the largest baryonic component, the hot plasma mapped in X-ray and SZ bands, in hydrostatic equilibrium.

The physical quantities directly observable are the density  $n_{\text{gas}}$  and temperature  $T_{\text{gas}}$  of the X-ray-emitting gas, and the SZ pressure profile  $P_{\text{gas}}$ . The gas density is obtained from the geometrical deprojection of the X-ray surface brightness in Fig. 1. Thanks to the observational strategy implemented in X-COP, we are able to correct the X-ray emission for the presence of clumps both by

masking substructures spatially resolved with *XMM-Newton* and by measuring the azimuthal median, instead of the azimuthal mean, out to  $\sim 1.2R_{200}$ , with a median relative uncertainty of 6 per cent and 1 per cent in Abell 2142 and Abell 2319, respectively. The estimates of the gas temperature are based on the modelling with an absorbed thermal component of the *XMM-Newton* spectra extracted from concentric annuli around the X-ray peak in the [0.5–12] keV energy band and corrected from the local sky background components (see Tchernin et al. 2016 for details). A typical statistical error lower than 5 per cent is associated with these spectral measurements, with a profile resolved in 12 bins out to 1.4 Mpc in Abell 2142 and in 14 bins out to 1.9 Mpc in Abell 2319. The SZ electron pressure profile is obtained from the deprojection of the azimuthally averaged integrated Comptonization parameter  $y$  extracted from a re-analysis of the SZ signal mapped with *Planck* (e.g. Planck Collaboration V 2013; Tchernin et al. 2016) and that extends up to  $\sim 3$  and 4 Mpc in Abell 2142 and Abell 2319, respectively. The electron density, temperature and SZ pressure profiles are presented in Fig. 2.

Under the assumption that the intracluster medium has a spherically symmetric distribution and follows the perfect gas law ( $P_{\text{gas}} = kT_{\text{gas}}n_{\text{gas}}$ , where  $k$  is Boltzmann’s constant and  $n_{\text{gas}}$  is the sum of the electron and proton densities  $n_e + n_p \approx 1.83n_e$ ), the gas density, combined with the X-ray spectral measurements of the gas temperature and/or the SZ-derived gas pressure, allows us to evaluate the total mass within a radius  $r$  through the hydrostatic equilibrium equation (see e.g. Ettori et al. 2013):

$$M_{\text{tot}}(<r) = -\frac{r P_{\text{gas}}}{\mu m_{\text{u}} G n_{\text{gas}}} \frac{d \log P_{\text{gas}}}{d \log r}, \quad (4)$$

where  $G$  is the gravitational constant,  $m_{\text{u}} = 1.66 \times 10^{-24}$  g is the atomic mass unit and  $\mu = 0.61$  is the mean molecular weight in atomic mass unit. In this analysis, we have applied both the *backward* and the *forward* methods. In the *backward* method, a parametric mass model is assumed and combined with the gas density profile to predict a gas temperature profile that is then compared, through, for example, a  $\chi^2$  minimization, with the one either measured in the spectral analysis or estimated as SZ  $P_{\text{gas}}/n_{\text{gas}}$  (losing the spatial resolution in the inner regions because of the modest 7 arcmin full width at half-maximum angular resolution of our

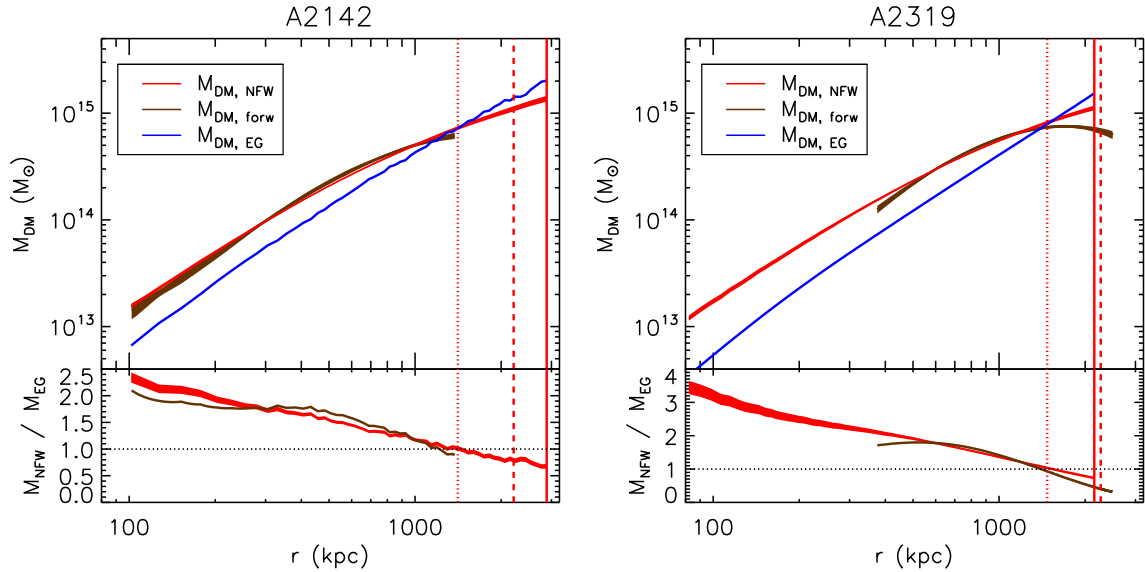


**Figure 3.** Dark matter profiles obtained using (i) the *backward* method with an NFW mass model; (ii) the *forward* method by fitting with functional forms the gas density profile and either the deprojected temperature profile (Abell 2142) or the SZ pressure profile (Abell 2319). In the latter case, the mass profiles are shown only within the radial range where the data are fitted. The dark matter profiles (blue curve) predicted from the ‘Emergent Gravity’ framework as obtained from equation (2) are also shown. The thickness of the lines shows the statistical uncertainty associated with the best-fitting mass model. Dotted/dashed/solid lines indicate the  $R_{500}/R_{200}$ /outermost radius of the extracted gas density profile, respectively, as estimated in the X-ray analysis. In the bottom panel, the ratio between the NFW mass model and  $M_{DM,EG}$  is shown.

*Planck* SZ maps, but gaining in radial extension due to the *Planck* spatial coverage; Planck Collaboration V 2013) to constrain the mass model parameters. Here, we combine both sets of constraints by summing up  $\chi^2_T = \sum_i^{N_x} (T_i - T_{mod,i})^2 / \epsilon_{T,i}^2$ , which is estimated from the spectral measurements of the gas temperature (and relative errors  $\epsilon_T$ ) resolved in  $N_x$  radial bins, and  $\chi^2_{SZ} = \Delta^T C^{-1} \Delta$ , which is evaluated from the SZ pressure profile resolved in  $N_{SZ}$  radial bins, by defining the elements of the matrix  $\Delta$  as  $\Delta_{ij} = P_i - P_{mod,j}$  and properly weighting by its covariance matrix  $C$ . In the present analysis, we adopt an NFW mass model with two free parameters: the mass concentration and  $R_{200}$ . This mass model provides a better representation (i.e. lower  $\chi^2$ ) of our data than any mass model including a central core. The statistical error associated with the mass is evaluated at each radius considering the range of the mass values allowed from the distribution of the best-fitting parameters within a  $\Delta\chi^2 = 2.3$ . The temperature and pressure profiles required from the best-fitting NFW mass model are shown in Fig. 2. In the *forward* method, some functional forms are fitted to the gas density profile and the deprojected gas temperature (or pressure) profile. The hydrostatic equilibrium equation (equation 4) is then directly applied to evaluate the radial distribution of the mass. The errors are estimated through a Monte Carlo process. The functional forms used to reproduce the profiles are a double  $\beta$ -model for the gas density (Cavaliere & Fusco-Femiano 1976), a six-parameter function for the temperature,  $T = p_0 (p_3 + (r/p_1)^{p_4}) / (1 + (r/p_1)^{p_4}) / (1 + (r/p_2)^{p_5})$  (e.g. Vikhlinin et al. 2006, Baldi et al. 2012) or a five-parameter generalized NFW for the pressure,  $P = p_0 / ((r/p_1)^{p_2} (1 + (r/p_1)^{p_3})^{(p_4 - p_2)/p_3})$  (e.g. Arnaud et al. 2010).

#### 4 RESULTS ON THE DARK MATTER MASS PROFILES

From equation (4), using a *backward* method with an NFW model, we measure in Abell 2142 a total mass of  $M_{500} = 8.7 \times 10^{14} M_\odot$ ,

with a relative statistical error of 3 per cent, and  $R_{200} = 2211 \pm 47$  kpc, with the gas density that extends up to  $r = 2890$  kpc. As discussed in Tchernin et al. (2016), the hydrostatic mass profile agrees well with the one obtained by weak-lensing and caustics measurements out to  $R_{200}$ . In Abell 2319, we measure  $M_{500} = 7.5 \times 10^{14} M_\odot$ , with a relative statistical error of 2 per cent, and  $R_{200} = 2084 \pm 13$  kpc, with the outermost radius for the gas density at 3 Mpc. A systematic uncertainty of about 10 per cent on these mass measurements is estimated by applying the *forward* method (with both the temperature and pressure profiles). The dark matter distribution is then  $M_{DM} = M_{tot} - M_B$ , where  $M_B$  is the baryonic mass estimated as described in Section 2.

In Fig. 3, we show the mass profiles obtained both in a context of a  $\Lambda$ CDM model and following the prescriptions for an emergent dark matter contribution. An encouraging match between the two mass profiles is obtained at  $r \approx R_{500}$ , where we measure  $M_{DM}/M_{DM,EG} = 1.01 \pm 0.04$  in Abell 2142 and  $0.81 \pm 0.02$  in Abell 2319, where the errors include only the propagation of the statistical uncertainties. In contrast,  $M_{DM,EG}$  underpredicts significantly, by up to a factor of 2–3, the requested amount of matter to maintain the hydrostatic equilibrium in the central regions,  $r < 200$  kpc. We conclude that, although the total masses within  $\approx R_{500}$  are in good agreement, the overall shape of the dark matter profiles looks quite different, with the Emergent Gravity lacking some NFW-type curvature.

By inverting the hydrostatic equilibrium equation, and assuming as boundary condition  $P_{out} = P(R_{500})$ , we can also estimate the gas temperature profiles that the computed  $M_{DM,EG}$  would imply for the measured gas density profiles. The tension below 1000 kpc can then be translated into a difference in the gas temperature of 2–4 keV, which can be hardly accommodated with the present observational constraints.<sup>1</sup>

<sup>1</sup> By comparing the predicted and the observed temperature profiles, we estimate a  $\Delta\chi^2$  between  $\sim 200$  (for Abell 2319) and 830 (Abell 2142) in

## 5 CONCLUSIONS

We have investigated the dark matter profiles in two massive X-ray luminous galaxy clusters for which the gas density and temperature (from *XMM-Newton* X-ray data) and SZ pressure profiles (from *Planck*) are recovered at a very high accuracy up to about  $R_{200}$ . By applying the hydrostatic equilibrium equation on these profiles, we constrain the dark matter distribution using different methods and models, obtaining results consistent within  $\sim 10$  per cent. Other systematic uncertainties might affect our mass reconstruction, such as any other (e.g. non-thermal) contribution to the total gas pressure (e.g. Nelson, Lau & Nagai 2014b; Sereno et al. 2017), other terms that account for departures from the hydrostatic equilibrium (e.g. Nelson et al. 2014a; Biffi et al. 2016) or the violation of the assumed sphericity of the gas distribution (e.g. Sereno et al. 2017). All these contributions have been shown to affect more significantly the clusters' outskirts and tend to bias higher (by 10–30 per cent) the total mass estimates at  $r > R_{500}$ , with lower effects in the inner regions. However, in Abell 2142, we observe an excellent agreement between the reconstructed mass profiles using X-ray, weak-lensing and galaxy dynamics (Tchernin et al. 2016), suggesting that, at least for this system, the hydrostatic equilibrium is a valid approximation allowing a robust constraint of the mass profile out to  $R_{200}$ .

Then, we compare those to  $M_{\text{DM,EG}}$ , the value predicted to play the role of an apparent dark matter as manifestation of an excess of gravity in the ‘Emergent Gravity’ scenario suggested in Verlinde (2016), which has the appealing property to depend only on the observed baryonic mass and the Hubble constant, with no extra free parameter. To this aim, we recover the baryonic mass as the sum of the observed gas mass and of the statistically estimated mass in stars. We observe that  $M_{\text{DM,EG}}$  reproduces well the dark matter distribution requested to maintain the gas in pressure equilibrium beyond 1 Mpc from the cluster core, with a remarkable good match at  $r \approx R_{500}$ , but presents significant discrepancies (by a factor of 2–3) in the innermost 200 kpc.

We note that any underestimate of the hydrostatic mass (of the order of 10 per cent or less, if any, in the latest analyses of samples of galaxy clusters, for example, Mahdavi et al. 2013; Donahue et al. 2014; Applegate et al. 2016; Smith et al. 2016; bias that we exclude in Abell 2142, as discussed in Tchernin et al. 2016) would imply a higher true mass at larger radii shifting the radius at which  $M_{\text{DM,EG}}$  and the expected dark matter value agree. Considering the extremely tight constraints on the gas density that come from the exquisite combination of high statistics and control of the systematics in the background modelling, the only way to reconcile this discrepancy would require a systematic overestimate of the gas temperature by 2–4 keV at  $r < 1000$  kpc, which is completely inconsistent with the present observational constraints, also accounting for potential systematics due to the calibration of the X-ray instruments (e.g. Schellenberger et al. 2015). Otherwise, this discrepancy might suggest that some temperature (or gas entropy) contribution, with an effect comparable with a modulation by some scale radius and larger in the inner cluster's regions, is still missing in Verlinde's formula. Massive (probably sterile) neutrinos can also accommodate this tension (e.g. Nieuwenhuizen 2016).

A larger sample of high-quality data, as the ones that will be available in the X-COP project in the near future, will improve the

statistical constraints on the reliability of any alternative scenario, as the ‘Emergent Gravity’.

## ACKNOWLEDGEMENTS

We thank the anonymous referee for helpful comments that improved the presentation of this work. This research has received funding from the European Union's Horizon 2020 Programme under AHEAD project (grant agreement no. 654215). We thank Guillaume Hurier to have generated the *Planck* SZ maps used in X-COP. SE acknowledges the financial support from contracts ASI-INAF I/009/10/0, NARO15 ASI-INAF I/037/12/0 and ASI 2015-046-R.0.

## REFERENCES

- Allen S. W., Evrard A. E., Mantz A. B., 2011, *ARA&A*, 49, 409  
 Applegate D. E. et al., 2016, *MNRAS*, 457, 1522  
 Arnaud M., Pratt G. W., Piffaretti R., Böhringer H., Croston J. H., Pointecouteau E., 2010, *A&A*, 517, A92  
 Baldi A., Ettori S., Molendi S., Gastaldello F., 2012, *A&A*, 545, A41  
 Biffi V. et al., 2016, *ApJ*, 827, 112  
 Brouwer M. M. et al., 2016, *MNRAS*, 466, 2547  
 Cavaliere A., Fusco-Femiano R., 1976, *A&A*, 49, 137  
 Diez-Tejedor A., Gonzalez-Morales A. X., Niz G., 2016, preprint (arXiv:1612.06282)  
 Donahue M. et al., 2014, *ApJ*, 794, 136  
 Eckert D. et al., 2014, *A&A*, 570, A119  
 Eckert D., Ettori S., Pointecouteau E., Molendi S., Paltani S., Tchernin C., 2017, *Astron. Nachr.*, 338, 293  
 Ettori S., Donnarumma A., Pointecouteau E., Reiprich T. H., Giodini S., Lovisari L., Schmidt R. W., 2013, *Space Sci. Rev.*, 177, 119  
 Farnsworth D., Rudnick L., Brown S., Brunetti G., 2013, *ApJ*, 779, 189  
 Ghizzardi S., Rossetti M., Molendi S., 2010, *A&A*, 516, A32  
 Gonzalez A. H., Sivanandam S., Zabludoff A. I., Zaritsky D., 2013, *ApJ*, 778, 14  
 Kravtsov A. V., Borgani S., 2012, *ARA&A*, 50, 353  
 Lin Y.-T., Mohr J. J., Stanford S. A., 2004, *ApJ*, 610, 745  
 Mahdavi A., Hoekstra H., Babul A., Bildfell C., Jeltema T., Henry J. P., 2013, *ApJ*, 767, 116  
 Milgrom M., Sanders R. H., 2016, preprint (arXiv:1612.09582)  
 Navarro J. F., Frenk C. S., White S. D. M., 1997, *ApJ*, 490, 493  
 Nelson K., Lau E. T., Nagai D., Rudd D. H. Yu L., 2014a, *ApJ*, 782, 107  
 Nelson K., Lau E. T., Nagai D., 2014b, *ApJ*, 792, 25  
 Nieuwenhuizen T. M., 2016, preprint (arXiv:1610.01543)  
 Oegerle W. R., Hill J. M., Fitchett M. J., 1995, *AJ*, 110, 32  
 Owers M. S., Nulsen P. E. J., Couch W. J., 2011, *ApJ*, 741, 122  
 Planck Collaboration I, 2011, *A&A*, 536, A1  
 Planck Collaboration V, 2013, *A&A*, 550, A131  
 Planck Collaboration XXIX, 2014, *A&A*, 571, A29  
 Schellenberger G., Reiprich T. H., Lovisari L., Nevalainen J., David L., 2015, *A&A*, 575, A30  
 Sereno M., Ettori S., Meneghetti M., Sayers J., Umetsu K., Merten J., Chiu I.-N., Zitrin A., 2017, *MNRAS*, 467, 3801  
 Smith G. P. et al., 2016, *MNRAS*, 456, L74  
 Storm E. et al., 2015, *AAS Meeting Abstracts*, 225, 304.05  
 Struble M. F., Rood H. J., 1999, *ApJS*, 125, 35  
 Sunyaev R. A., Zel'dovich Y. B., 1972, *Comments Astrophys. Space Phys.*, 4, 173  
 Tchernin C. et al., 2016, *A&A*, 595, A42  
 Verlinde E. P., 2016, preprint (arXiv:1611.02269)  
 Vikhlinin A., Kravtsov A., Forman W., Jones C. Markevitch M., Murray S. S., Van S. L., 2006, *ApJ*, 640, 691

disfavour of the  $M_{\text{DM,EG}}$ . The null hypothesis that the NFW model, with two free parameters, does not provide a better representation of the data than the Emergent Gravity, with no free parameters, is excluded at  $>99$  per cent.

This paper has been typeset from a  $\text{\LaTeX}$  file prepared by the author.